

Structural stability, electronic structure, and magnetic properties of the single-layer trilayer $\text{La}_3\text{Ni}_2\text{O}_7$ polymorph

Shekhar Sharma,^{1,*} Yi-Feng Zhao,^{1,†} and Antia S. Botana¹

¹*Department of Physics, Arizona State University, Tempe, AZ 85287, USA*

(Dated: January 23, 2026)

A polymorph of the bilayer nickelate $\text{La}_3\text{Ni}_2\text{O}_7$ that displays an alternating single-layer and trilayer (1313) stacking pattern has recently been discovered. Signatures of superconductivity under pressure have been found in this novel phase. At ambient pressure, $\text{La}_3\text{Ni}_2\text{O}_7$ -1313 has been reported to crystallize in three different space group symmetries $Cmmm$, $Imma$, and $Fmmm$. Unlike the commonly observed tilted NiO_6 octahedra in perovskite nickelates, the $Cmmm$ phase exhibits no NiO_6 tilts, implying that this structural feature alone may be insufficient to give rise to superconductivity in Ruddlesden-Popper nickelates. Here, we employ first-principles calculations and group theory analysis to study the pressure dependence of the structural instabilities in this single-layer trilayer $\text{La}_3\text{Ni}_2\text{O}_7$ polymorph. At ambient pressure, we identify multiple unstable phonon branches in the highest symmetry ($Cmmm$) structure at various high-symmetry points of the Brillouin zone. Distortions associated with these instabilities lead to one of the other experimentally reported space groups ($Imma$), that does display octahedral tilts. The magnetic tendencies indicate that the electronic structure of $\text{La}_3\text{Ni}_2\text{O}_7$ -1313 at ambient pressure is dominated by the trilayer block, as the single-layer is in a Mott-insulating regime. Under pressure, a tetragonal $P4/mmm$ structure becomes stable, in agreement with experiments.

I. INTRODUCTION

Since the discovery of the cuprates [1], there have been several attempts at identifying new high- T_c materials with cuprate-like characteristics [2]. Given the proximity of nickel to copper in the periodic table, nickelates have been considered prime candidates in this context [3–7]. By drawing analogies with the cuprates in terms of their crystal structure and $3d$ electron count, superconductivity in nickelates was first discovered in epitaxial thin films of the reduced square-planar phases $\text{R}_{n+1}\text{Ni}_n\text{O}_{2n+2}$ (R = rare-earth), characterized by a cuprate-like sequence of $n\text{-NiO}_2$ layers separated by fluorite RO_2 blocks along the c -axis [8–11]. These phases have a Ni oxidation state close to 1+, isovalent to Cu^{2+} , and they display an electronic structure characterized by the dominant role of $d_{x^2-y^2}$ bands, in a cuprate-like fashion [12–17]. Within this family, both the infinite-layer ($n = \infty$) compounds RNiO_2 ($\text{R} = \text{La, Pr, Nd}$) [18–21] and the quintuple-layer ($n = 5$) $\text{Nd}_6\text{Ni}_5\text{O}_{12}$ material [22] have been shown to be superconducting with similar $T_c \sim 15$ K.

A significant breakthrough in the field occurred in 2023 with the observation of superconductivity under pressure in the parent Ruddlesden-Popper (RP) $\text{R}_{n+1}\text{Ni}_n\text{O}_{3n+1}$ phases [23–27], characterized by a sequence of $n\text{-NiO}_6$ perovskite layers separated by rocksalt RO blocks along the c -axis [28]. The first superconducting signatures were reported in the bilayer ($n = 2$) RP nickelate $\text{La}_3\text{Ni}_2\text{O}_7$ [23, 25]. This material has been shown to exhibit a $T_c \sim 80$ K within a pressure range of ~ 14.0 to 40 GPa [23, 25]. Concomitant with the emergence of

superconductivity, a structural transition from orthorhombic $Amam$ at ambient pressure to $Fmmm$ (or tetragonal $I4/mmm$) under pressure has been reported [23, 29]. This transition is associated with a change in the out-of-plane Ni-O-Ni bond angle from $\sim 168.0^\circ$ to 180.0° . The electronic structure of this material is characterized by the active role of bands of $d_{x^2-y^2}$ and d_{z^2} character. Many studies have suggested that the straightening of the Ni-O-Ni bond angle along the c -axis with pressure is related to the emergence of superconductivity due to the associated enhancement in d_{z^2} inter-layer coupling via the apical oxygens [30–40].

Recently, a new polymorph of $\text{La}_3\text{Ni}_2\text{O}_7$ was reported [41–44]. In contrast to the typical uniform bilayer (2222) stacking of perovskite blocks of $\text{La}_3\text{Ni}_2\text{O}_7$, the structure of this polymorph consists of a novel sequence of alternating single-layer and trilayer blocks forming a 1313 configuration. Superconductivity in this new $\text{La}_3\text{Ni}_2\text{O}_7$ -1313 polymorph has also been reported under pressure with a T_c as high as that of $\text{La}_3\text{Ni}_2\text{O}_7$ -2222 [42, 44, 45]. An anomaly in the resistivity of $\text{La}_3\text{Ni}_2\text{O}_7$ -1313 occurs at ~ 180 K [41, 45]. A kink has also been identified at a similar temperature in the magnetic susceptibility [45]. This anomaly is hence similar to that detected in the conventional bilayer $\text{La}_3\text{Ni}_2\text{O}_7$ -2222 [46] and the trilayer $\text{La}_4\text{Ni}_3\text{O}_{10}$ [26], suggesting a possible spin density wave (SDW) transition in the 1313 $\text{La}_3\text{Ni}_2\text{O}_7$ polymorph. In $\text{La}_3\text{Ni}_2\text{O}_7$ -2222, all experimental studies (neutrons, RIXS, NMR, and μ SR) agree on a SDW propagation vector $q = (0.25, 0.25)$ (in pseudotetragonal notation) with two possible stripe models: a double-spin stripe or a single charge-spin stripe [47–51]. In the trilayer $\text{La}_4\text{Ni}_3\text{O}_{10}$ neutron data were taken to test for the presence of a SDW concomitant with the charge-density wave [52]. The intensity distribution of the derived superlattice reflections is consistent with a rather unusual magnetic state: outer

* sshar246@asu.edu

† yzhao421@asu.edu

planes that are antiferromagnetically coupled and no moment on the inner planes. The slight incommensurability of the SDW ordering vector results in an approximate 5-period stripe in the plane.

The crystal structure of the $\text{La}_3\text{Ni}_2\text{O}_7$ -1313 polymorph at ambient pressure remains ambiguous as it can reasonably be refined within different space groups due to the presence of weak reflections in the home-lab X-ray diffraction data [41–43]. Chen *et al.* found that $\text{La}_3\text{Ni}_2\text{O}_7$ -1313 crystallizes in an orthorhombic space group, with reflection conditions consistent with *Cmmm* symmetry for most of their crystals, although they note evidence for a competing *Imma* variant [41]. Wang *et al.* similarly concluded that this new polymorph is best described in a *Cmmm* space group [43]. In contrast, Puphal *et al.* reported that an *Fmmm* space group provides the best refinement instead [42]. Importantly, the *Cmmm* structure of ambient-pressure $\text{La}_3\text{Ni}_2\text{O}_7$ -1313 (that is non-superconducting) displays 180° Ni-O-Ni out-of-plane bond angles in the trilayer block, implying that this structural feature alone may be insufficient to give rise to superconductivity. Hence, it is important to understand if the *Cmmm* structure is indeed the most feasible one for this new nickelate polymorph or if the *Imma* or *Fmmm* structures (that do contain octahedral tilts) are more stable instead. The electronic structure of the *Fmmm* and *Cmmm* phases has been scrutinized in some previous work and it seems to show some similarities and differences with the 2222 counterpart [44, 53–55]. ARPES data taken on pure $\text{La}_3\text{Ni}_2\text{O}_7$ -1313 single crystals indicate an electronic structure for this polymorph that is analog to that of the isolated trilayer $\text{La}_4\text{Ni}_3\text{O}_{10}$ [56].

To shed light on the differing data reported for $\text{La}_3\text{Ni}_2\text{O}_7$ -1313, here we study the structural properties and the related electronic structure of this material as a function of pressure using first-principles calculations and symmetry analysis. We start by investigating the structural stability of the experimental structure with higher-symmetry at ambient pressure (*Cmmm*) and explore the symmetry connections with the other reported space groups symmetries for this material. Our lattice dynamics calculations reveal that the *Cmmm* phase exhibits multiple instabilities. Using group theory analysis, we find that the distortions associated with the irreducible representations (irreps) of the unstable phonon branches could transform the *Cmmm* structure into different space groups, including the experimentally reported *Imma*. Under pressure, we find that the tetragonal *P4/mmm* structure becomes stable, consistent with experiments. The magnetic tendencies indicate that the electronic structure of $\text{La}_3\text{Ni}_2\text{O}_7$ -1313 at ambient pressure is dominated by the trilayer block as the single-layer is in a Mott-insulating state, consistent with ARPES [56].

II. COMPUTATIONAL METHODS

Structural optimizations for $\text{La}_3\text{Ni}_2\text{O}_7$ -1313 in the different space group symmetries and at different pressures were performed using density functional theory (DFT) non-spin-polarized calculations with the Vienna *ab-initio* Simulation Package (VASP) [57–59]. Both the internal coordinates and the lattice parameters were relaxed using the Perdew-Burke-Ernzerhof (PBE) version of the generalized gradient approximation (GGA) as the exchange correlation functional [60]. A k -mesh of $10 \times 10 \times 4$ was used for the *Cmmm* structure, while k -meshes of $4 \times 4 \times 2$ were used for both the *Imma* and *Fmmm* structures. A force convergence criterion of 10^{-4} eV/Å and an energy cutoff of 520 eV were employed in all cases.

Phonon dispersion calculations for the *Cmmm* structure were carried out using Density Functional Perturbation Theory (DFPT), as implemented in the VASP-DFPT package Phonopy [61]. A unit cell of size $2 \times 2 \times 1$ was chosen. An energy convergence criteria of 10^{-8} eV and a k -mesh of $4 \times 4 \times 1$ was used. To analyze the unstable phonon branches and their irreps, we used the ISODISTORT module of the ISOTROPY software suite [62, 63]. The character tables for each irrep were examined using the Bilbao Crystallographic Server [64, 65], and the visualization of crystal structures was performed with the VESTA software [66].

Subsequently, spin-polarized electronic-structure calculations were performed for both the *Cmmm* and *Imma* structures also using VASP. An energy cut-off of 400 eV and a k -mesh of $4 \times 4 \times 2$ were used to sample the Brillouin zone. To study the magnetic tendencies at ambient pressure, we employed the rotationally invariant LDA + U method [67]. We analyzed the U dependence of the energetics for different magnetic configurations using on-site Coulomb repulsion U values of 3, 4 and 5 eV while the Hund's rule coupling value (J) was fixed to 0.7 eV.

III. EXPERIMENTAL CRYSTAL STRUCTURE

The experimental crystal structure of $\text{La}_3\text{Ni}_2\text{O}_7$ -1313 in the three different space groups reported (*Cmmm*, *Imma*, and *Fmmm*) is shown in Fig. 1 wherein the single-layer+trilayer structure of this polymorph can be clearly observed. There are three inequivalent Ni atoms in the structure: one from the single-layer block (SL) and two from the trilayer that we call inner layer (IL) and outer layer (OL). The relevant Ni-O bond lengths are highlighted in Fig. 1. The in-plane and out-of-plane Ni-O bond lengths in the *Cmmm* and *Imma* structures are very similar and also consistent with those reported for the individual structural components, namely, the single layer La_2NiO_4 and trilayer $\text{La}_4\text{Ni}_3\text{O}_{10}$ nickelates (see Appendix A). In contrast, the Ni-O bond lengths of the experimentally-resolved *Fmmm* structure can be seen to be markedly different. For both the *Imma* and *Fmmm* structures, the trilayer block exhibits clear octahedral tilts

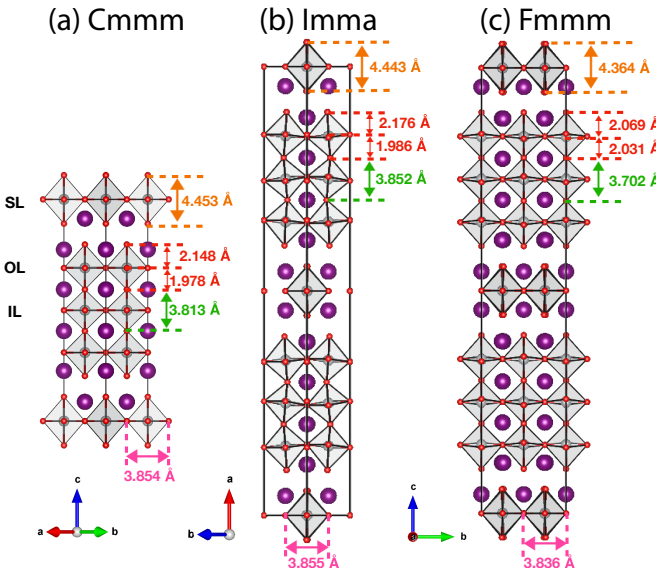


FIG. 1. Crystal structure of $\text{La}_3\text{Ni}_2\text{O}_7$ -1313 in the three experimentally reported space groups *Cmmm*, *Imma*, and *Fmmm*. Spheres in purple, gray, and red represent the La, Ni, and O atoms, respectively. The single-layer block is denoted by SL while the outer layer and inner layer within the trilayer are denoted as OL and IL, respectively. The in-plane and out-of-plane Ni-O bond lengths are shown explicitly.

TABLE I. Irreducible representations (irreps), frequencies, order parameter directions (OPDs) and the corresponding transformed structures for the lowest-frequency unstable phonon modes at the Y and T points for *Cmmm*- $\text{La}_3\text{Ni}_2\text{O}_7$ -1313.

k-points	Frequency (meV)	OPD	Structure
Y	$\text{Y}_2^+ ; 18.28i$	(a)	Pbam
	$\text{Y}_3^+ ; 14.00i$	(a)	Pmna
	$\text{Y}_4^+ ; 13.66i$	(a)	Pmna
T	$\text{T}_1^- ; 18.44i$	(a)	Ibam
	$\text{T}_4^- ; 13.89i$	(a)	Imma
	$\text{T}_3^- ; 13.56i$	(a)	Imma

with a Ni-O-Ni out-of-plane angle of 166.48° for *Imma* and 171.42° for *Fmmm*. Due to the out-of-plane NiO_6 octahedral tilts, the *Imma* and *Fmmm* unit cells are doubled along the out-of-plane direction compared to the *Cmmm* structure where, as mentioned above, the Ni-O-Ni bond angle across the apical oxygens is 180° . The NiO_6 octahedra in the single-layer block remain untilted across all three space groups.

IV. RESULTS

A. Structural Stability

We start by analyzing the dynamical stability of the crystal structure with higher symmetry at ambient pressure for $\text{La}_3\text{Ni}_2\text{O}_7$ -1313 (*Cmmm*) by studying its phonon

dispersion, shown in Fig. 2(a). We perform our phonon analysis for $\text{La}_3\text{Ni}_2\text{O}_7$ -1313 in the nonmagnetic state as analog calculations in $\text{La}_3\text{Ni}_2\text{O}_7$ -2222 and $\text{La}_4\text{Ni}_3\text{O}_{10}$ give rise to stable phonon dispersions in their respective experimentally reported structures with *Amam* and *P2₁/c* symmetries [68, 69]. In contrast, the calculated phonon dispersion for the *Cmmm* structure of $\text{La}_3\text{Ni}_2\text{O}_7$ -1313 exhibits several instabilities, the lower ones in energy being along the Brillouin zone edge Y-T (see Fig. 2(a)).

The largest instability in the phonon dispersion corresponds to a nondegenerate branch with irreps Y_2^+ and T_1^- at the Y and T points, respectively. Subsequently, an almost doubly-degenerate branch can be observed with irreps Y_3^+ , Y_4^+ and T_4^- , T_3^- . These branches are almost dispersionless along Y-T. Higher in energy lies another quasi-degenerate branch (with stronger dispersion along Y-T) with irreps Y_3^- , Y_4^- and T_3^+ , T_4^+ . The distortion patterns of each irrep at the T point of the Brillouin zone are shown in Fig. 2(b) (the analog distortions at the Y point are shown in Appendix B). The distortion due to the T_1^- irrep corresponds to an in-plane rotation of oxygen atoms of the inner layer of the trilayer block. The T_4^- and T_3^- modes mainly involve tilting of the NiO_6 octahedra of the trilayer blocks about the [100] and [010] axis respectively, without introducing any displacements in the single-layer block. As such, the T_4^- and T_3^- distortions lead to a Ni-O-Ni apical bond angle different from 180° . The mode with T_3^+ irrep involves an out-of-plane rotation of the NiO_6 octahedra about the [100] axis while the T_4^+ involves a rotation about the [010] axis. In addition to the NiO_6 octahedral rotation of the trilayer block, the modes with T_3^+ and T_4^+ irreps also lead to the rotation of the NiO_6 octahedra of the single-layer block about the [100] axis for T_3^+ and about the [010] axis for T_4^+ .

We now focus on the imaginary frequencies of the lowest-frequency phonon modes at Y and T that are listed in Table I (details on the rest of the modes are shown in Appendix B). Table I also shows the space group symmetry of the structures obtained using the distortions associated with each of the irreps of these most unstable phonon modes for the *Cmmm* structure at both Y and T. It is important to note that the distortions associated to the irreps at the Y point never lead to crystal structures with *Fmmm* or *Imma* symmetry (the other two experimentally reported space groups). In contrast, the distortions associated with the T_4^- and T_3^- irreps can lead to a structure with *Imma* symmetry. The distortions associated with T_3^+ and T_4^+ irreps also lead to an *Imma* structure, even though these do not correspond to the lowest-frequency modes.

After studying its dynamical stability at ambient pressure, we now make enthalpy considerations for $\text{La}_3\text{Ni}_2\text{O}_7$ -1313 in relation to the proposed space group symmetries. We note that enthalpy calculations from first-principles in the nonmagnetic state for $\text{La}_3\text{Ni}_2\text{O}_7$ -2222 and $\text{La}_4\text{Ni}_3\text{O}_{10}$ have revealed the transition from an orthorhombic (*Amam*) or monoclinic (*P2₁/c*) crystal setting to a tetragonal (*I4/mmm*) structure under pres-

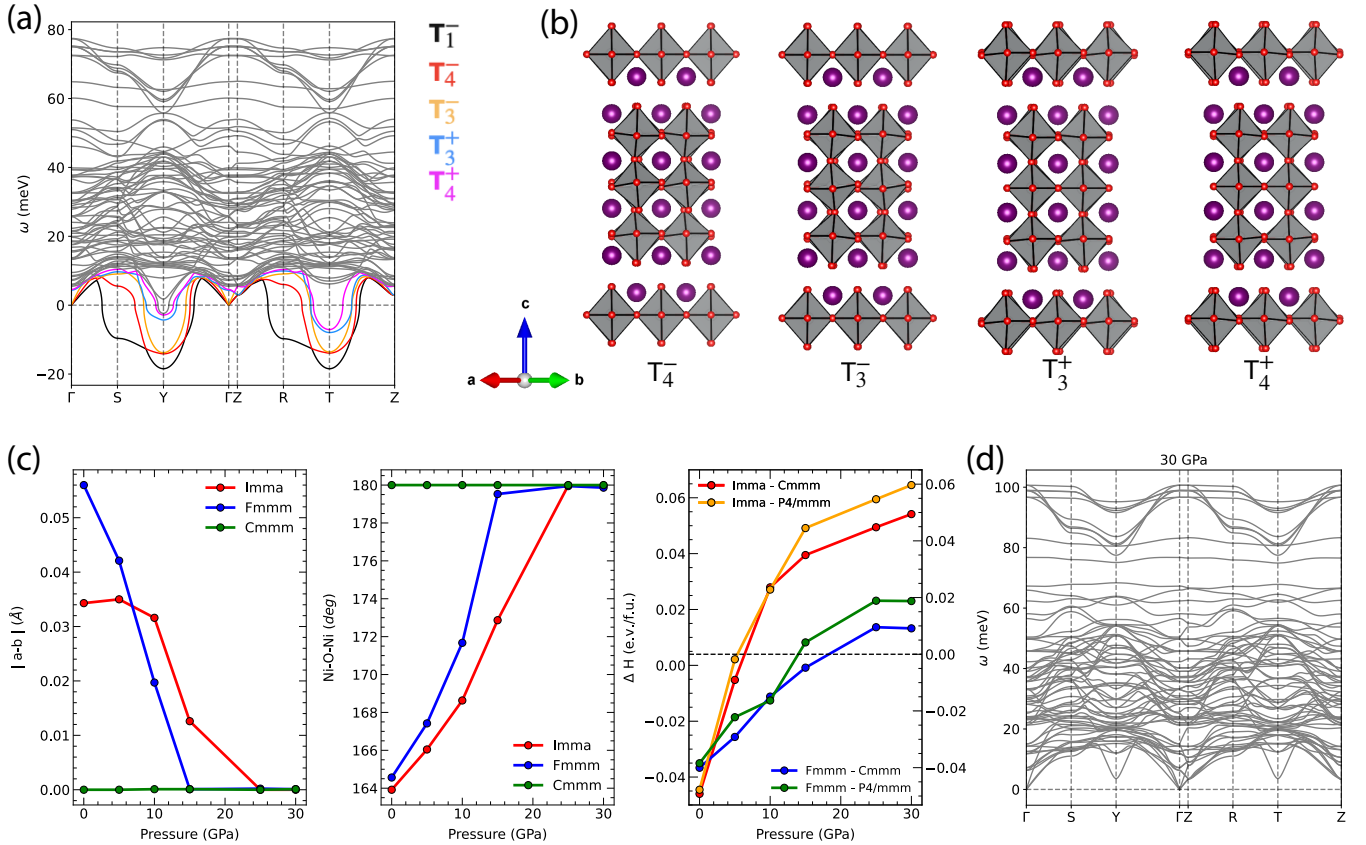


FIG. 2. (a) Phonon dispersion of *Cmmm*-La₃Ni₂O₇-1313 at ambient pressure. The different unstable modes at various high symmetry points of the *Cmmm* Brillouin zone are highlighted with different colors. The high symmetry points correspond to: Γ = (0.0, 0.0, 0.0), S = (0.0, 0.5, 0.0), Y = (0.5, 0.5, 0.0), Z = (0.0, 0.0, 0.5), R = (0.0, 0.5, 0.5), T = (0.5, 0.5, 0.5). (b) Distortions associated with each of the four irreps of the unstable phonon branches at T that lead to an *Imma* structure: T_4^- , T_3^- , T_3^+ , and T_4^+ . (c) (left) Evolution of the lattice parameters of the *Cmmm*, *Imma*, and *Fmmm* structures with pressure. (middle) Evolution of the Ni-O-Ni bond angle across the apical oxygen with pressure for the three different space groups. (right) Enthalpy (H = E + PV) evolution of *Imma* and *Fmmm* structures with respect to the *Cmmm* (left y-scale) and *P4/mmm* (right y-scale) structures. At ambient pressure the *Imma* structure has the lowest enthalpy. The *P4/mmm* space group becomes more stable at ~ 13 GPa, consistent with experiments. (d) Phonon dispersion of the *P4/mmm* structure at 30 GPa that is dynamically stable. All the first-principles results in this figure correspond to fully relaxed structures and non-spin-polarized calculations.

sure [38, 68], in agreement with XRD data [29, 70, 71]. Analog calculations in La₃Ni₂O₇-1313 (see Fig. 2(c)) reveal the same type of transition with a *P4/mmm* structure quickly becoming more stable once pressure is applied (using any experimentally reported space group symmetry as a starting point), also in agreement with experiments [42]. Across the transition, the difference between the *a* and *b* lattice constants becomes zero, leading to a tetragonalized crystal structure at ~ 15 GPa for an *Fmmm* and at 25 GPa for an *Imma* space group as a starting point. Concomitantly, the Ni-O-Ni apical bond angles straighten to 180°. This finding is consistent with the phonon calculations that show that, with increasing pressure, the soft phonon branches harden leading to a dynamically stable crystal structure with *P4/mmm* symmetry at ~ 30 GPa (see Fig. 2(d) and a full pressure evolution in Appendix C). Importantly, the enthalpy results at ambient pressure

seem to reinforce the likelihood of a structure containing octahedral tilts at ambient pressure in La₃Ni₂O₇-1313. At 0 GPa, the *Imma* is the most stable structure, with an energy approximately 40 meV/f.u. lower than that of the *Cmmm* structure. The *Fmmm* structure is also more stable than the *Cmmm* one but it is less stable than the *Imma*.

To summarize, our analysis of the unstable phonon branches in the experimentally reported structure with higher-symmetry at ambient pressure for La₃Ni₂O₇-1313 (*Cmmm*) shows that this structure can transform into one of the other experimentally reported space groups (*Imma*) through the distortions associated to irreps at the T point (an *Fmmm* structure cannot be obtained from any of the lowest-frequency modes). Enthalpy considerations also seem to favor an *Imma* space group symmetry. Therefore, based on our analysis, the *Imma* structure seems to be

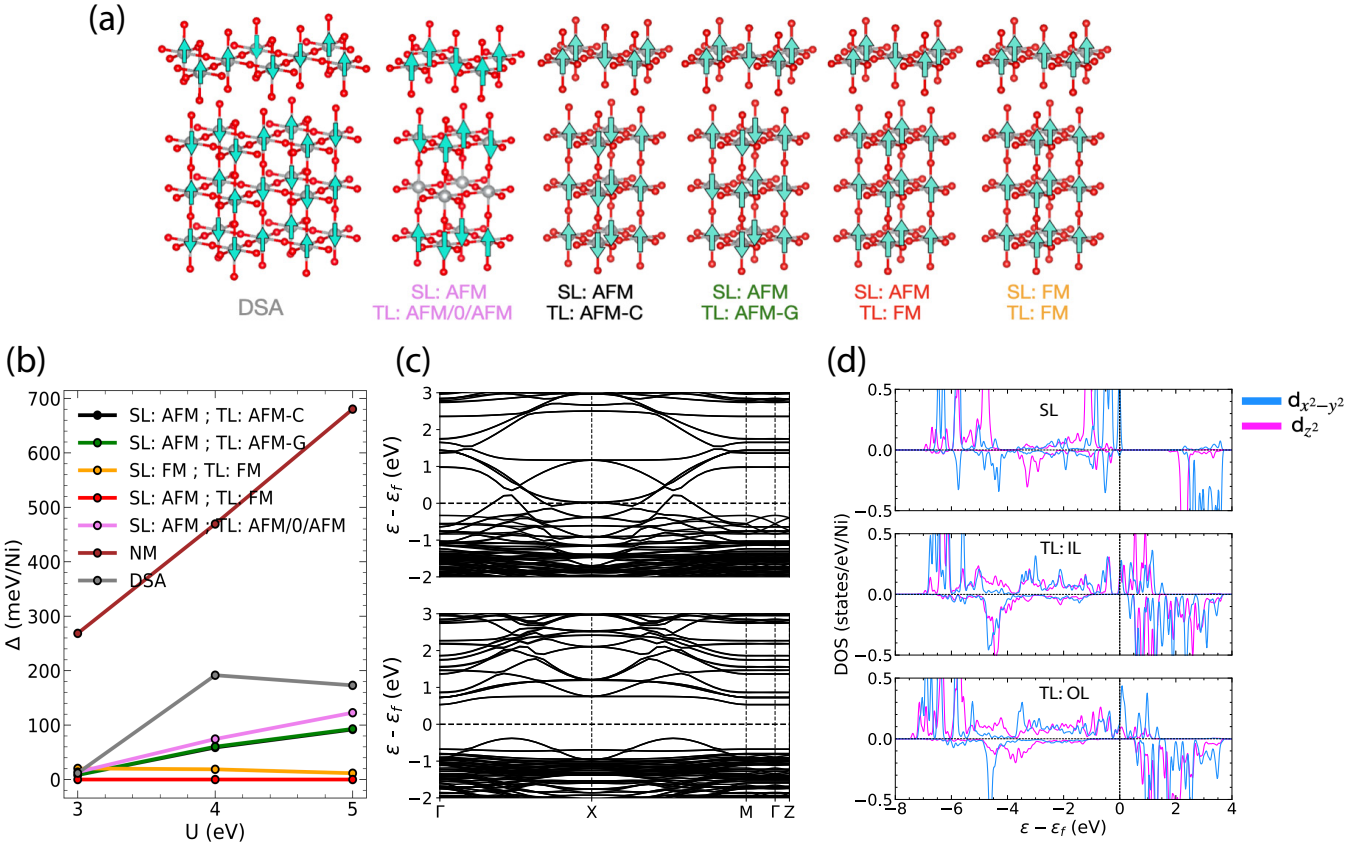


FIG. 3. Magnetic tendencies of *Imma*-La₃Ni₂O₇-1313 at ambient pressure. (a) Spin configurations analyzed in this work. SL denotes the single-layer, TL the trilayer Ni atoms. (b) Energetics of the different magnetic configurations as a function of U . (c) Band structure for the ground state configuration (SL:AFM; TL:FM) at $U = 4$ eV in both the majority and minority spin channel. (d) Orbitally (e_g) projected density of states for SL, TL:IL (inner-layer) and TL:OL (outer-layer) Ni atoms in the magnetic ground state (d_{z^2} pink, $d_{x^2-y^2}$ blue).

the most feasible one out of the three experimentally reported structures for La₃Ni₂O₇-1313, indicating that this hybrid phase (akin to the conventional bilayer and trilayer compounds) likely contains octahedral tilts.

Some final remarks about the structural stability of La₃Ni₂O₇-1313 are in order. While based on our symmetry analysis and on energetics, the *Imma* structure seems to be the most feasible one out of the three experimentally reported ones, it is important to note that the *Imma* structure involves condensation of only the quasi-doubly-degenerate branch at T in the phonon dispersion shown in Fig. 2(a). Using not only individual irreps of the unstable phonon modes but also their sum with each other, other structures can be generated that involve condensation of not only the quasi-doubly-degenerate branch but also the nondegenerate (most unstable) branch, as done in Ref. [72]. However, we have found that such structures (for example *Pnma*) do not provide an energy gain. Further, while it would be useful to perform similar structural stability studies in spin-polarized calculations (as done for La₃Ni₂O₇-2222 [73]), the lack of information about the q of the density wave state in the single-layer trilayer

polymorph prevents us from doing such an analysis in a meaningful manner at this point.

B. Electronic structure and magnetic properties

After achieving a basic understanding of the structural stability of La₃Ni₂O₇-1313 (that points to the presence of octahedral tilts), we now explore magnetic tendencies in this material to scrutinize its low-energy electronic structure. In the nonmagnetic state at the DFT level (as reported by us and others [41, 54]), the single-layer bands cross the Fermi level. This result disagrees with recent ARPES experiments [56] that find a Fermi surface analog to that of the trilayer nickelate La₄Ni₃O₁₀, with the single-layer bands being out of the picture. To shed light on this issue, we performed LDA+ U calculations for different magnetic configurations for a range of U s from 3 to 5 eV in both *Cmmm* and *Imma* space group symmetries. The magnetic configurations we attempted (depicted in Fig. 3(a)) are: a) a double spin-stripe (DSA), analog of the magnetic ground state of La₃Ni₂O₇-2222,

b) A checkerboard antiferromagnetic configuration in the single-layer and an antiferromagnetic-C-type configuration in the trilayer (SL: AFM; TL: AFM-C). c) A checkerboard antiferromagnetic state in the single-layer and an antiferromagnetic-G-type configuration in the trilayer (SL: AFM; TL: AFM-G). d) A ferromagnetic single-layer and ferromagnetic trilayer (SL: FM; TL: FM). e) A checkerboard antiferromagnetic configuration in the single-layer and a ferromagnetic configuration in the trilayer (SL: AFM; TL: FM). f) A checkerboard AFM configuration in the single-layer as well as in the outer-layers of the trilayer, with the inner-layer of the trilayer having zero moments (SL: AFM TL: AFM/0/AFM). This latter magnetic state, with a node in the inner layer of the trilayer and antiferromagnetically coupled outer layers (in agreement with neutron data [52]) has been shown to be the magnetic ground state for the trilayer nickelate $\text{La}_4\text{Ni}_3\text{O}_{10}$ from DFT for a $\sqrt{2} \times \sqrt{2}$ -sized cell [68, 74]. While we analyze all of these magnetic states in *Cmmm* and *Imma* space group symmetries, we present in the main text the results for the *Imma* structure only (the *Cmmm* results are shown in Appendix D). Regardless of the space group chosen, the SL: AFM; TL: FM is the magnetic ground state for all U values analyzed here for the magnetic states and cell sizes we analyze (see Fig. 3(b) and Appendix D). We emphasize once again that $\text{La}_3\text{Ni}_2\text{O}_7$ -1313 has a density-wave instability as reflected in the ambient-pressure transport data [41, 45] but information on the nature of the density-wave state and its q would be needed in order to further scrutinize that possibility from first-principles in appropriate/larger supercells.

The electronic structure for the magnetic ground state we obtain for $\text{La}_3\text{Ni}_2\text{O}_7$ -1313 is consistent with ARPES data in terms of the dominance of the trilayer block. Fig. 3 (c, d) shows the electronic band structure and e_g -density of states for this SL: AFM; TL: FM configuration at $U = 4$ eV. As expected, given the average $d^{7.5}$ filling for the Ni atoms, orbitals of d_{z^2} and $d_{x^2-y^2}$ character dominate the electronic structure around the Fermi level, with most of the weight at the Fermi energy coming from the planar $d_{x^2-y^2}$ orbitals. Importantly, the DOS of the single-layer Ni is clearly gapped as a consequence of the AFM order in the plane (and the inclusion of an on-site Coulomb repulsion), in line with the Mott insulating state of La_2NiO_4 [75]. As a consequence, only states from the trilayer Ni atoms are relevant at the Fermi level. The derived magnetic moments in the magnetic ground state at $U = 4$ eV are $\sim 1.5 \mu_B$ for the single layer nickel, $\sim 1.4 \mu_B$ for the outer layer Ni of the trilayer and a reduced $\sim 1.2 \mu_B$ for the inner nickel of the trilayer block (further information on the evolution of the magnetic moments can be seen in Appendix D). These derived moments are consistent with a higher d occupation for the single-layer Ni atoms. The moments disproportionate

within the trilayer block, indicating a different effective doping for inner and outer planes, as shown in previous work for $\text{La}_4\text{Ni}_3\text{O}_{10}$ [68]. The electronic structure we just described for $\text{La}_3\text{Ni}_2\text{O}_7$ -1313 is in agreement with DFT+DMFT calculations in $\text{La}_3\text{Ni}_2\text{O}_7$ -1313 that show that when dynamical correlations are taken into account, the single-layer block is in a Mott-insulating regime [55]. More importantly, our results, as mentioned above, are in accordance with recent ARPES data that show that the low-energy physics of this material is very similar to that of the ‘isolated’ trilayer $\text{La}_4\text{Ni}_3\text{O}_{10}$ system [56]. Indeed, the unfolded band structure of our magnetic ground state is very similar to that of the trilayer material [76], as shown in Appendix E. As the electronic structure at high-pressure in *P4/mmm* symmetry has been intensively studied in previous work [44, 53–55], we do not analyze it here.

V. CONCLUSIONS

In summary, we have employed first-principles methods and group theory analysis to study the structure and electronic structure of the newly discovered single-layer-trilayer $\text{La}_3\text{Ni}_2\text{O}_7$ polymorph. At ambient pressure, the structure of this material in the experimentally reported space group with higher symmetry (*Cmmm*) exhibits multiple unstable phonon branches. Distortions associated with these instabilities lead to one of the other experimentally reported space groups (*Imma*), that is the most stable space group at ambient pressure also from enthalpy considerations. Importantly, the *Imma* structure contains octahedral tilts, indicating that the hybrid $\text{La}_3\text{Ni}_2\text{O}_7$ -1313 polymorph is likely structurally similar to the conventional bilayer and trilayer RP phases. Under pressure, a *P4/mmm* structure becomes stable, in agreement with XRD experiments. The magnetic tendencies at ambient pressure show that the electronic structure of $\text{La}_3\text{Ni}_2\text{O}_7$ -1313 in its magnetic ground state is dominated by the trilayer block as the single-layer is in a Mott insulating regime. This is in agreement with recent ARPES data. Our results beg for a more detailed analysis of the ambient pressure structure of $\text{La}_3\text{Ni}_2\text{O}_7$ -1313 from synchrotron or neutron diffraction to clarify the presence of octahedral tilts. Further experiments to determine the nature (and propagation vector) of the apparent density-wave state should also be pursued to clarify the magnetic ground state of this material and its connection to the conventional bilayer and trilayer RPs.

ACKNOWLEDGEMENTS

We acknowledge NSF grant No. DMR-2045826 and the ASU research computing center for HPC resources.

[1] J. G. Bednorz and K. A. Müller, Possible high T_c superconductivity in the Ba–La–Cu–O system, *Z. Phys. B* **64**, 189 (1986).

[2] M. R. Norman, Materials design for new superconductors, *Rep. Prog. Phys.* **79**, 074502 (2016).

[3] V. I. Anisimov, D. Bakhvalov, and T. M. Rice, Electronic structure of possible nickelate analogs to the cuprates, *Phys. Rev. B* **59**, 7901 (1999).

[4] K.-W. Lee and W. E. Pickett, Infinite-layer LaNiO_2 : Ni^{1+} is not Cu^{2+} , *Phys. Rev. B* **70**, 165109 (2004).

[5] J. Chaloupka and G. Khaliullin, Orbital order and possible superconductivity in $\text{LaNiO}_3/\text{LaMO}_3$ superlattices, *Phys. Rev. Lett.* **100**, 016404 (2008).

[6] P. Hansmann, X. Yang, A. Toschi, G. Khaliullin, O. K. Andersen, and K. Held, Turning a Nickelate Fermi Surface into a Cupratelike One through Heterostructuring, *Phys. Rev. Lett.* **103**, 016401 (2009).

[7] M. J. Han, X. Wang, C. A. Marianetti, and A. J. Millis, Dynamical Mean-Field Theory of Nickelate Superlattices, *Phys. Rev. Lett.* **107**, 206804 (2011).

[8] X. Zhou, P. Qin, Z. Feng, H. Yan, X. Wang, H. Chen, Z. Meng, and Z. Liu, Experimental progress on the emergent infinite-layer Ni-based superconductors, *Mater. Today* **55**, 170 (2022).

[9] B. Y. Wang, K. Lee, and B. H. Goodge, Experimental progress in superconducting nickelates, *Annu. Rev. Condens. Matter Phys.* **15**, 305 (2024).

[10] J. F. Mitchell, A nickelate renaissance, *Front. Phys.* **9**, 813483 (2021).

[11] Q. Gu and H.-H. Wen, Superconductivity in nickel-based 112 systems, *Innovation* **3**, 100202 (2022).

[12] A. S. Botana and M. R. Norman, Similarities and differences between LaNiO_2 and CaCuO_2 and implications for superconductivity, *Phys. Rev. X* **10**, 011024 (2020).

[13] M. Hepting, D. Li, C. J. Jia, H. Lu, E. Paris, Y. Tseng, X. Feng, M. Osada, E. Been, Y. Hikita, Y.-D. Chuang, Z. Hussain, K. J. Zhou, A. Nag, M. Garcia-Fernandez, M. Rossi, H. Y. Huang, D. J. Huang, Z. X. Shen, T. Schmitt, H. Y. Hwang, B. Moritz, J. Zaanan, T. P. Devereaux, and W. S. Lee, Electronic structure of the parent compound of superconducting infinite-layer nickelates, *Nat. Mater.* **19**, 381 (2020).

[14] M. Kitatani, L. Si, P. Worm, J. M. Tomczak, R. Arita, and K. Held, Optimizing superconductivity: From cuprates via nickelates to palladates, *Phys. Rev. Lett.* **130**, 166002 (2023).

[15] P. Jiang, L. Si, Z. Liao, and Z. Zhong, Electronic structure of rare-earth infinite-layer RNiO_2 ($\text{R} = \text{La}, \text{Nd}$), *Phys. Rev. B* **100**, 201106(R) (2019).

[16] A. S. Botana, K.-W. Lee, M. R. Norman, V. Pardo, and W. E. Pickett, Low valence nickelates: Launching the nickel age of superconductivity, *Front. Phys.* **9**, 813532 (2022).

[17] H. LaBollita and A. S. Botana, Electronic structure and magnetic properties of higher-order layered nickelates: $\text{La}_{n+1}\text{Ni}_n\text{O}_{2n+2}$ ($n = 4 - 6$), *Phys. Rev. B* **104**, 035148 (2021).

[18] D. Li, K. Lee, B. Y. Wang, M. Osada, S. Crossley, H. R. Lee, Y. Cui, Y. Hikita, and H. Y. Hwang, Superconductivity in an infinite-layer nickelate, *Nature* **572**, 624 (2019).

[19] M. Osada, B. Y. Wang, B. H. Goodge, K. Lee, H. Yoon, K. Sakuma, D. Li, M. Miura, L. F. Kourkoutis, and H. Y. Hwang, A superconducting praseodymium nickelate with infinite layer structure, *Nano Lett.* **20**, 5735 (2020).

[20] M. Osada, B. Y. Wang, K. Lee, D. Li, and H. Y. Hwang, Phase diagram of infinite layer praseodymium nickelate $\text{Pr}_{1-x}\text{Sr}_x\text{NiO}_2$ thin films, *Phys. Rev. Mater.* **4**, 121801(R) (2020).

[21] D. Li, B. Y. Wang, K. Lee, S. P. Harvey, M. Osada, B. H. Goodge, L. F. Kourkoutis, and H. Y. Hwang, Superconducting dome in $\text{Nd}_{1-x}\text{Sr}_x\text{NiO}_2$ infinite layer films, *Phys. Rev. Lett.* **125**, 027001 (2020).

[22] G. A. Pan, D. Ferenc Segedin, H. LaBollita, Q. Song, E. M. Nica, B. H. Goodge, A. T. Pierce, S. Doyle, S. Novakov, D. Córdova Carrizales, A. T. N'Diaye, P. Shafer, H. Paik, J. T. Heron, J. A. Mason, A. Yacoby, L. F. Kourkoutis, O. Erten, C. M. Brooks, A. S. Botana, and J. A. Mundy, Superconductivity in a quintuple-layer square-planar nickelate, *Nat. Mater.* **21**, 160 (2022).

[23] H. Sun, M. Huo, X. Hu, J. Li, Z. Liu, Y. Han, L. Tang, Z. Mao, P. Yang, and B. Wang, Signatures of superconductivity near 80 K in a nickelate under high pressure, *Nature* **621**, 493 (2023).

[24] N. Wang, G. Wang, X. Shen, J. Hou, J. Luo, X. Ma, H. Yang, L. Shi, J. Dou, and J. Feng, Bulk high-temperature superconductivity in pressurized tetragonal $\text{La}_2\text{PrNi}_2\text{O}_7$, *Nature* **634**, 579 (2024).

[25] J. Hou, P.-T. Yang, Z.-Y. Liu, J.-Y. Li, P.-F. Shan, L. Ma, G. Wang, N.-N. Wang, H.-Z. Guo, J.-P. Sun, Y. Uwatoko, M. Wang, G.-M. Zhang, B.-S. Wang, and J.-G. Cheng, Emergence of high-temperature superconducting phase in pressurized $\text{La}_3\text{Ni}_2\text{O}_7$ crystals, *Chin. Phys. Lett.* **40**, 117302 (2023).

[26] Y. Zhu, D. Peng, E. Zhang, B. Pan, X. Chen, L. Chen, H. Ren, F. Liu, Y. Hao, N. Li, Z. Xing, F. Lan, J. Han, J. Wang, D. Jia, H. Wo, Y. Gu, Y. Gu, L. Ji, W. Wang, H. Gou, Y. Shen, T. Ying, X. Chen, W. Yang, H. Cao, C. Zheng, Q. Zeng, J. Guo, and J. Zhao, Superconductivity in pressurized trilayer $\text{La}_4\text{Ni}_3\text{O}_{10-\delta}$ single crystals, *Nature* **631**, 531 (2024).

[27] Q. Li, Y.-J. Zhang, Z.-N. Xiang, Y. Zhang, X. Zhu, and H.-H. Wen, Signature of superconductivity in pressurized $\text{La}_4\text{Ni}_3\text{O}_{10}$, *Chin. Phys. Lett.* **41**, 017401 (2024).

[28] M. Greenblatt, Ruddlesden–popper $\text{Ln}_{n+1}\text{Ni}_n\text{O}_{3n+1}$ nickelates: structure and properties, *Curr. Opin. Solid State Mater. Sci.* **2**, 174 (1997).

[29] L. Wang, Y. Li, S.-Y. Xie, F. Liu, H. Sun, C. Huang, Y. Gao, T. Nakagawa, B. Fu, and B. Dong, Structure responsible for the superconducting state in $\text{La}_3\text{Ni}_2\text{O}_7$ at high-pressure and low-temperature conditions, *J. Am. Chem. Soc.* **146**, 7506 (2024).

[30] Z. Luo, X. Hu, M. Wang, W. Wú, and D.-X. Yao, Bilayer two-orbital model of $\text{La}_3\text{Ni}_2\text{O}_7$ under pressure, *Phys. Rev. Lett.* **131**, 126001 (2023).

[31] Y. Zhang, L.-F. Lin, A. Moreo, and E. Dagotto, Electronic structure, dimer physics, orbital-selective behavior, and magnetic tendencies in the bilayer nickelate superconductor $\text{La}_3\text{Ni}_2\text{O}_7$ under pressure, *Phys. Rev. B* **108**, L180510 (2023).

[32] Q.-G. Yang, D. Wang, and Q.-H. Wang, Possible s_{\pm} -wave superconductivity in $\text{La}_3\text{Ni}_2\text{O}_7$, *Phys. Rev. B* **108**,

[L140505 \(2023\)](#).

[33] Q.-G. Yang, K.-Y. Jiang, D. Wang, H.-Y. Lu, and Q.-H. Wang, Effective model and s_{\pm} -wave superconductivity in trilayer nickelate $\text{La}_4\text{Ni}_3\text{O}_{10}$, *Phys. Rev. B* **109**, L220506 (2024).

[34] H. Sakakibara, N. Kitamine, M. Ochi, and K. Kuroki, Possible high T_c superconductivity in $\text{La}_3\text{Ni}_2\text{O}_7$ under high pressure through manifestation of a nearly half-filled bilayer hubbard model, *Phys. Rev. Lett.* **132**, 106002 (2024).

[35] V. Christiansson, F. Petocchi, and P. Werner, Correlated electronic structure of $\text{La}_3\text{Ni}_2\text{O}_7$ under pressure, *Phys. Rev. Lett.* **131**, 206501 (2023).

[36] F. Lechermann, J. Gondolf, S. Bötzsel, and I. M. Eremin, Electronic correlations and superconducting instability in $\text{La}_3\text{Ni}_2\text{O}_7$ under high pressure, *Phys. Rev. B* **108**, L201121 (2023).

[37] M. Zhang, H. Sun, Y.-B. Liu, Q. Liu, W.-Q. Chen, and F. Yang, s_{\pm} -wave superconductivity in pressurized $\text{La}_4\text{Ni}_3\text{O}_{10}$, *Phys. Rev. B* **110**, L180501 (2024).

[38] Y. Zhang, L.-F. Lin, A. Moreo, T. A. Maier, and E. Dagotto, Structural phase transition, s_{\pm} -wave pairing, and magnetic stripe order in bilayered superconductor $\text{La}_3\text{Ni}_2\text{O}_7$ under pressure, *Nat. Commun.* **15**, 2470 (2024).

[39] C. Lu, Z. Pan, F. Yang, and C. Wu, Interlayer-coupling-driven high-temperature superconductivity in $\text{La}_3\text{Ni}_2\text{O}_7$ under pressure, *Phys. Rev. Lett.* **132**, 146002 (2024).

[40] J. Yang, H. Sun, X. Hu, Y. Xie, T. Miao, H. Luo, H. Chen, B. Liang, W. Zhu, G. Qu, C.-Q. Chen, M. Huo, Y. Huang, S. Zhang, F. Zhang, F. Yang, Z. Wang, Q. Peng, H. Mao, G. Liu, Z. Xu, T. Qian, D.-X. Yao, M. Wang, L. Zhao, and X. J. Zhou, Orbital-dependent electron correlation in double-layer nickelate $\text{La}_3\text{Ni}_2\text{O}_7$, *Nat. Commun.* **15**, 4373 (2024).

[41] X. Chen, Z. Zhang, A. S. Thind, S. Sharma, H. LaBollita, G. Peterson, H. Zheng, D. P. Phelan, A. S. Botana, R. F. Klie, and J. F. Mitchell, Polymorphism in the ruddlesden-popper nickelate $\text{La}_3\text{Ni}_2\text{O}_7$: Discovery of a hidden phase with distinctive layer stacking, *J. Am. Chem. Soc.* **146**, 6 (2024).

[42] P. Puphal, P. Reiss, N. Enderlein, Y.-M. Wu, G. Khalilu, V. Sundaramurthy, T. Priessnitz, M. Knauf, A. Suthar, L. Richter, M. Isobe, P. A. van Aken, H. Takagi, B. Keimer, Y. E. Suyolcu, B. Wehinger, P. Hansmann, and M. Hepting, Unconventional crystal structure of the high-pressure superconductor $\text{La}_3\text{Ni}_2\text{O}_7$, *Phys. Rev. Lett.* **133**, 146002 (2024).

[43] H. Wang, L. Chen, A. Rutherford, H. Zhou, and W. Xie, Long-range structural order in a hidden phase of ruddlesden-popper bilayer nickelate $\text{La}_3\text{Ni}_2\text{O}_7$, *Inorg. Chem.* **63**, 5020–5026 (2024).

[44] S. Abadi, K.-J. Xu, E. G. Lomeli, P. Puphal, M. Isobe, Y. Zhong, A. V. Fedorov, S.-K. Mo, M. Hashimoto, D.-H. Lu, B. Moritz, B. Keimer, T. P. Devoreaux, M. Hepting, and Z.-X. Shen, Electronic structure of the alternating monolayer-trilayer phase of $\text{La}_3\text{Ni}_2\text{O}_7$, *Phys. Rev. Lett.* **134**, 126001 (2025).

[45] C. Huang, J. Li, X. Huang, H. Zhang, D. Hu, M. Huo, X. Chen, Z. Chen, H. Sun, and M. Wang, Superconductivity in monolayer-trilayer phase of $\text{La}_3\text{Ni}_2\text{O}_7$ under high pressure, [arXiv:2510.12250](#) (2025).

[46] J. Li, D. Peng, P. Ma, H. Zhang, Z. Xing, X. Huang, C. Huang, M. Huo, D. Hu, Z. Dong, X. Chen, T. Xie, H. Dong, H. Sun, Q. Zeng, H.-k. Mao, and M. Wang, Identification of superconductivity in bilayer nickelate $\text{La}_3\text{Ni}_2\text{O}_7$ under high pressure up to 100 GPa, *Nat. Sci. Rev.* **12** (2025).

[47] N. K. Gupta, R. Gong, Y. Wu, M. Kang, C. T. Parzyck, B. Z. Gregory, N. Costa, R. Sutarto, S. Sarker, A. Singer, D. G. Schaom, K. M. Shen, and D. G. Hawthorn, Anisotropic spin stripe domains in bilayer $\text{La}_3\text{Ni}_2\text{O}_7$, *Nat. Commun.* **16**, 6560 (2025).

[48] X. Chen, J. Choi, Z. Jiang, J. Mei, K. Jiang, J. Li, S. Agrestini, M. Garcia-Fernandez, H. Sun, X. Huang, D. Shen, M. Wang, J. Hu, Y. Lu, K.-J. Zhou, and D. Feng, Electronic and magnetic excitations in $\text{La}_3\text{Ni}_2\text{O}_7$, *Nat. Commun.* **15**, 9597 (2024).

[49] K. Chen, X. Liu, J. Jiao, M. Zou, C. Jiang, X. Li, Y. Luo, Q. Wu, N. Zhang, Y. Guo, and L. Shu, Evidence of spin density waves in $\text{La}_3\text{Ni}_2\text{O}_{7-\delta}$, *Phys. Rev. Lett.* **132**, 256503 (2024).

[50] T. Xie, M. Huo, X. Ni, F. Shen, X. Huang, H. Sun, H. C. Walker, D. Adroja, D. Yu, B. Shen, L. He, K. Cao, and M. Wang, Strong interlayer magnetic exchange coupling in $\text{La}_3\text{Ni}_2\text{O}_{7-\delta}$ revealed by inelastic neutron scattering, *Science Bulletin* **69**, 3221 (2024).

[51] M. Kakoi, T. Oi, Y. Ohshita, M. Yashima, K. Kuroki, T. Kato, H. Takahashi, S. Ishiwata, Y. Adachi, N. Hatada, T. Uda, and H. Mukuda, Multiband metallic ground state in multilayered nickelates $\text{La}_3\text{Ni}_2\text{O}_7$ and $\text{La}_4\text{Ni}_3\text{O}_{10}$ probed by ^{139}La -NMR at ambient pressure, *J. Phys. Soc. Jpn.* **93**, 053702 (2024).

[52] J. Zhang, D. Phelan, A. S. Botana, Y.-S. Chen, H. Zheng, M. Krogstad, S. G. Wang, Y. Qiu, J. A. Rodriguez-Rivera, R. Osborn, S. Rosenkranz, M. R. Norman, and J. F. Mitchell, Intertwined density waves in a metallic nickelate, *Nat. Commun.* **11**, 6003 (2020).

[53] F. Lechermann, S. Bötzsel, and I. M. Eremin, Electronic instability, layer selectivity, and fermi arcs in $\text{La}_3\text{Ni}_2\text{O}_7$, *Phys. Rev. Mater.* **8**, 074802 (2024).

[54] Y. Zhang, L.-F. Lin, A. Moreo, T. A. Maier, and E. Dagotto, Electronic structure, self-doping, and superconducting instability in the alternating single-layer trilayer stacking nickelates $\text{La}_3\text{Ni}_2\text{O}_7$, *Phys. Rev. B* **110**, L060510 (2024).

[55] H. LaBollita, S. Bag, J. Kapeghian, and A. S. Botana, Electronic correlations, layer distinction, and electron doping in the alternating single-layer–trilayer $\text{La}_3\text{Ni}_2\text{O}_7$ polymorph, *Phys. Rev. B* **110**, 155145 (2024).

[56] C. C. Au-Yeung, X. Chen, S. Smit, M. Bluschke, V. Zimmermann, M. Michiardi, P. Moen, J. Kraan, C. S. B. Pang, C. T. Suen, S. Zhdanovich, M. Zonno, S. Gorovikov, Y. Liu, G. Levy, I. S. Elfimov, M. Berciu, G. A. Sawatzky, J. F. Mitchell, and A. Damascelli, Universal electronic structure of layered nickelates via oxygen-centered planar orbitals, [arXiv:2502.20450](#) (2025).

[57] G. Kresse and J. Hafner, Ab initio molecular dynamics for open-shell transition metals, *Phys. Rev. B* **48**, 13115 (1993).

[58] G. Kresse and J. Furthmüller, Efficiency of ab-initio total energy calculations for metals and semiconductors using a plane-wave basis set, *Comput. Mater. Sci.* **6**, 15 (1996).

[59] P. E. Blöchl, Projector augmented-wave method, *Phys. Rev. B* **50**, 17953 (1994).

[60] J. P. Perdew, K. Burke, and M. Ernzerhof, Generalized gradient approximation made simple, *Phys. Rev. Lett.* **77**, 3865 (1996).

[61] A. Togo and I. Tanaka, First principles phonon calculations in materials science, *Scr. Mater.* **108**, 1 (2015).

[62] H. T. Stokes, D. M. Hatch, and B. J. Campbell, Isotropy software suite, *Isotropy Software Suite* .

[63] B. J. Campbell, H. T. Stokes, D. E. Tanner, and D. M. Hatch, Isodisplace: An internet tool for exploring structural distortions, *J. Appl. Cryst.* **39**, 607 (2006).

[64] D. Orobengoa, C. Capillas, M. I. Aroyo, and J. M. Perez-Mato, *AMPLIMODES*: symmetry-mode analysis on the Bilbao Crystallographic Server, *J. Appl. Cryst.* **42**, 820 (2009).

[65] M. I. Aroyo, A. Kirov, C. Capillas, J. M. Perez-Mato, and H. Wondratschek, Bilbao Crystallographic Server. II. Representations of crystallographic point groups and space groups, *Acta Crystallogr. A* **62**, 115 (2006).

[66] K. Momma and F. Izumi, VESTA 3 for three-dimensional visualization of crystal, volumetric and morphology data, *J. Appl. Cryst.* **44**, 1272 (2011).

[67] S. L. Dudarev, G. A. Botton, S. Y. Savrasov, C. J. Humphreys, and A. P. Sutton, Electron-energy-loss spectra and the structural stability of nickel oxide: An LSDA + U study, *Phys. Rev. B* **57**, 1505 (1998).

[68] H. LaBollita, J. Kapeghian, M. R. Norman, and A. S. Botana, Electronic structure and magnetic tendencies of trilayer $\text{La}_4\text{Ni}_3\text{O}_{10}$ under pressure: Structural transition, molecular orbitals, and layer differentiation, *Phys. Rev. B* **109**, 195151 (2024).

[69] D. Puggioni and J. M. Rondinelli, Crystal structure stability and electronic properties of the layered nickelate $\text{La}_4\text{Ni}_3\text{O}_{10}$, *Phys. Rev. B* **97**, 115116 (2018).

[70] N. Li, J. Guan, L. Yan, X. Yan, M. Li, X. Liu, K. Zhang, F. Li, S. Cai, H. Dong, A. N-Diaye, M. Amboage, J. Zhang, Y. Cao, H. Guo, Q. Kong, L. Sun, and W. Yang, Crystal and electronic structure studies of $\text{La}_4\text{Ni}_3\text{O}_{10-\delta}$ under high-pressure and low-temperature conditions, *J. Am. Chem. Soc.* **147**, 43717 (2025).

[71] H. Wang, H. Zhou, and W. Xie, Temperature-dependent structural evolution of ruddlesden–popper bilayer nickelate $\text{La}_3\text{Ni}_2\text{O}_7$, *Inorg. Chem.* **64**, 828 (2025).

[72] A. Subedi, Pressure-tunable structural instabilities in single-layer-trilayer $\text{La}_3\text{Ni}_2\text{O}_7$, *arXiv:2412.21150* (2024).

[73] X.-W. Yi, Y. Meng, J.-W. Li, Z.-W. Liao, W. Li, J.-Y. You, B. Gu, and G. Su, Nature of charge density waves and metal-insulator transition in pressurized $\text{La}_3\text{Ni}_2\text{O}_7$, *Phys. Rev. B* **110**, L140508 (2024).

[74] Y. Zhang, L.-F. Lin, A. Moreo, T. A. Maier, and E. Dagotto, Prediction of s^\pm -wave superconductivity enhanced by electronic doping in trilayer nickelates $\text{La}_4\text{Ni}_3\text{O}_{10}$ under pressure, *Phys. Rev. Lett.* **133**, 136001 (2024).

[75] G. W. Guo and W. M. Temmerman, Electronic structure and magnetism in La_2NiO_4 , *J. Phys. C: Solid State Phys.* **21**, L803 (1988).

[76] H. Li, X. Zhou, T. Nummy, J. Zhang, V. Pardo, W. E. Pickett, J. F. Mitchell, and D. S. Dessau, Fermiology and electron dynamics of trilayer nickelate $\text{La}_4\text{Ni}_3\text{O}_{10}$, *Nat. Commun.* **8**, 704 (2017).

[77] S. J. Skinner, Characterisation of $\text{La}_2\text{NiO}_{4+\delta}$ using in-situ high temperature neutron powder diffraction, *Solid State Sci.* **5**, 419 (2003).

[78] J. Zhang, H. Zheng, Y.-S. Chen, Y. Ren, M. Yonemura, A. Huq, and J. F. Mitchell, High oxygen pressure floating zone growth and crystal structure of the metallic nickelates $\text{R}_4\text{Ni}_3\text{O}_{10}$ ($\text{R} = \text{La, Pr}$), *Phys. Rev. Mater.* **4**, 083402 (2020).

[79] M. Chen and M. Weinert, Layer k -projection and unfolding electronic bands at interfaces, *Phys. Rev. B* **98**, 245421 (2018).

[80] M. X. Chen and M. Weinert, Revealing the substrate origin of the linear dispersion of silicene/ $\text{Ag}(111)$, *Nano Lett.* **14**, 5189 (2014).

Appendix A: Structural data for La_2NiO_4 and $\text{La}_4\text{Ni}_3\text{O}_{10}$

Fig. 4 shows the structural data for La_2NiO_4 and $\text{La}_4\text{Ni}_3\text{O}_{10}$ extracted from Refs. [77, 78] in order to compare the relevant bond lengths of the two individual structural components with those of $\text{La}_3\text{Ni}_2\text{O}_7$ -1313 shown in Fig. 1.

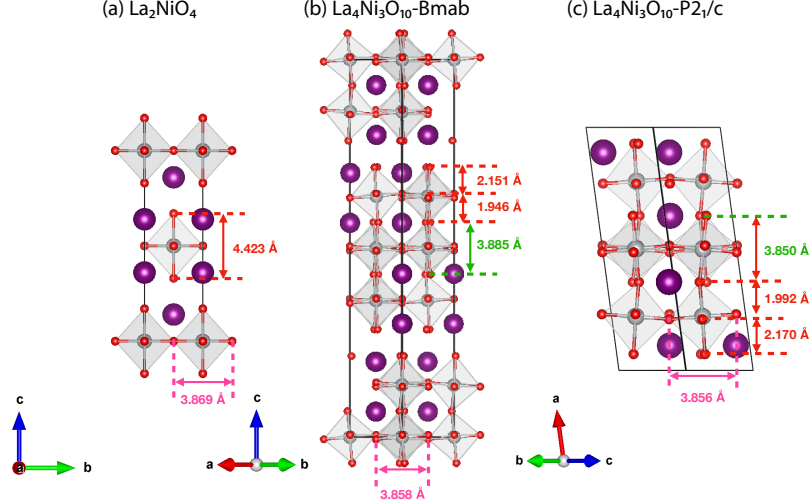


FIG. 4. Structures of (a) La_2NiO_4 and of $\text{La}_4\text{Ni}_3\text{O}_{10}$ in both $Bmab$ (b) and $P2_1/c$ (c) symmetries. Relevant bond lengths as obtained from experimental structural data are shown.

Appendix B: Further details on the unstable phonon branches for the $Cmmm$ structure

Table II shows a complete list of irreps, frequencies, OPDs and corresponding distorted structures for all unstable phonon modes of $Cmmm$ - $\text{La}_3\text{Ni}_2\text{O}_7$ -1313. Fig. 5 shows the displacement patterns of high-symmetry modes at the Y and T points of the Brillouin zone, as described in the main text, as well as at the S and R points. At the S point, the distortion mode corresponds to S_1^- whose displacement patterns lead to the tilting of NiO_6 octahedra of the trilayer block about both the [100] and [010] in-plane axis. The octahedra of the single-layer block remain undistorted. At the R point, the unstable normal mode has irrep R_1^+ . Similarly to S_1^- , the displacement patterns lead to the rotation of the trilayer block about both the [100] and [010] axis which ultimately leads to the out-of-plane tilting of NiO_6 octahedra. Note that via distortions at R, an $Fmmm$ structure could be obtained.

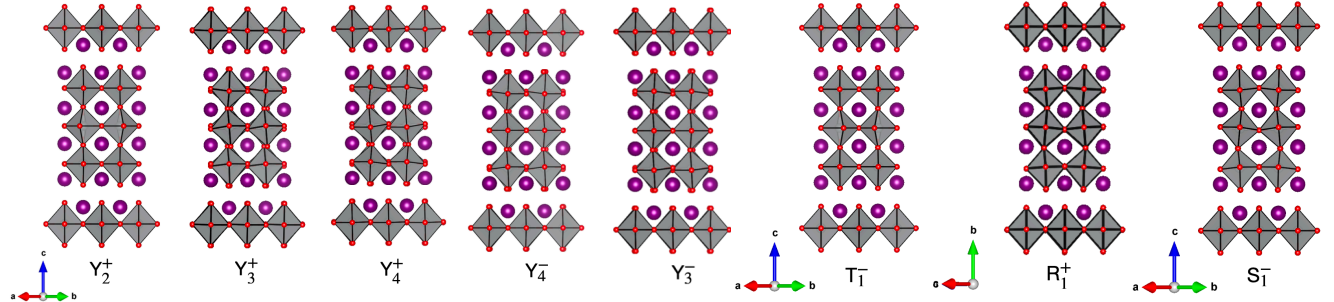


FIG. 5. Distortions corresponding to the irreps of the unstable phonon branches of $Cmmm$ - $\text{La}_3\text{Ni}_2\text{O}_7$ -1313 at the Y, T, R, and S points of the Brillouin zone not shown in the main text.

TABLE II. Complete set of irreducible representations (irreps), frequencies, order parameter directions (OPDs) and the corresponding transformed structures for all unstable phonon modes for $Cmmm$ - $\text{La}_3\text{Ni}_2\text{O}_7$ -1313.

k-point	Frequency (meV)	OPD	Structure	k-point	Frequency (meV)	OPD	Structure
S	S_1^- ; $9.58i$	(a,0), (a,b)	P2/c	R	R_1^+ ; $9.65i$	(a,0), (a,b) (a,a)	C2/m Fmmm
Y	Y_2^+ ; $18.28i$	(a)	Pbam	T	T_1^- ; $18.44i$	(a)	Ibam
	Y_3^+ ; $14.00i$, $2.83i$	(a)	Pmna		T_4^- ; $13.89i$	(a)	Imma
	Y_4^+ ; $13.66i$	(a)	Pmna		T_3^- ; $13.56i$	(a)	Imma
	Y_3^- ; $2.35i$	(a)	Pmma		T_3^+ ; $7.94i$	(a)	Imma
	Y_4^- ; $4.27i$	(a)	Pmma		T_4^+ ; $7.07i$	(a)	Imma

Appendix C: Phonon dispersions in $P4/mmm$ symmetry

Fig. 6 shows the evolution with pressure of the phonon dispersion of $\text{La}_3\text{Ni}_2\text{O}_7$ -1313 in $P4/mmm$ symmetry. $Fmmm$, $Cmmm$, and $Imma$ structures can be obtained from the $P4/mmm$ phase via atomic displacements associated with the irreps of different unstable phonon modes (see Table III). Similar to the $Cmmm$ structure, at ambient pressure, there are two unstable phonon branches at M (the most unstable branch being nondegenerate and the other being doubly degenerate). At A there is an extra doubly degenerate phonon branch. As shown in Table III, the most (nondegenerate) unstable branch has irreps M_2^+ and A_4^- at M and A, respectively. The subsequent doubly degenerate branch has irreps M_5^+ and A_5^- . The following doubly-degenerate branch at A has the same irrep. The M_2^+ (and A_4^-) modes involve predominantly an in-plane rotation of the middle layer of the NiO_6 octahedra within the trilayer. The M_5^+ (and A_5^-) modes involve rotation of all the NiO_6 octahedra in planes parallel to the c axis, similar to the leading instabilities of the $Cmmm$ phase described in the main text. With increasing pressure, the unstable branches are gradually suppressed, as shown in Fig. 6.

TABLE III. Irreducible representations (irreps), frequencies, order parameter directions (OPDs) and the corresponding transformed structures of the two lowest-frequency unstable phonon branches at the M and A points of the Brillouin zone for $P4/mmm$ - $\text{La}_3\text{Ni}_2\text{O}_7$ -1313.

k-points	Frequency (meV)	OPD	Structure
M	M_2^+ ; $17.66i$	(a)	P4/mbm
	M_5^+ ; $12.70i$	(a,0)	Pmna
		(a,a)	Cmma
		(a,b)	P2/c
A	A_4^- ; $17.70i$	(a)	I4/mcm
	A_5^- ; $12.09i$	(a,0)	Imma
		(a,a)	Fmmm
		(a,b)	C2/m

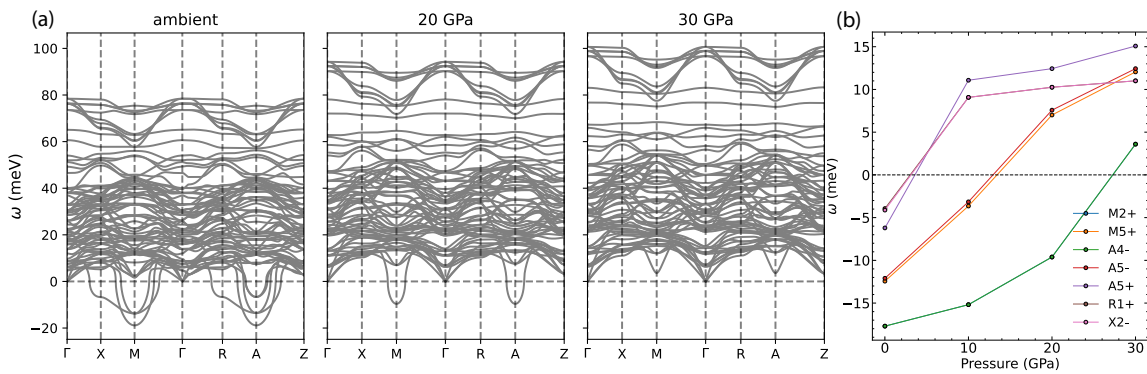


FIG. 6. (a) Evolution of the phonon dispersion of $P4/mmm$ - $\text{La}_3\text{Ni}_2\text{O}_7$ -1313 with pressure. (Left panel) ambient pressure, (middle panel) 20 GPa, (right panel) 30 GPa. (b) Evolution of different distortion modes with pressure. M_2^+ , A_4^- and R_1^+ , X_2^- are degenerate and their plots coincide.

TABLE IV. Magnetic moments of the inequivalent Ni atoms (in μ_B) for *Imma*-La₃Ni₂O₇-1313 for the different magnetic states depicted in Fig. 3 as a function of U . SL denotes the single-layer Ni atoms, OL the outer-layer Ni atoms within the trilayer, and IL the inner-layer Ni atoms within the trilayer.

U (eV)	DSA	SL: AFM	SL: AFM	SL: AFM	SL: AFM	SL: FM
		TL: AFM/0/AFM	TL: AFM-C	TL: AFM-G	TL: FM	TL: FM
3	SL: 0.430/ -0.430	SL: 1.395/ -1.395	SL: 1.370/ -1.370	SL: 1.359/ -1.359	SL: 1.400/ -1.424	SL: 1.532
	OL: 1.195/ -1.195	OL: 1.093/ -1.093	OL: 1.109/ -1.109	OL: 1.103/ -1.103	OL: 1.323	OL: 1.367
	IL: 0.586/ -0.586	IL: 0.000	IL: 0.507/ -0.507	IL: 0.505/ -0.505	IL: 1.020	IL: 1.024
4	SL: 0.314/ -0.314	SL: 1.478/ -1.478	SL: 1.457/ -1.457	SL: 1.448/ -1.448	SL: 1.469/ -1.455	SL: 1.579
	OL: 1.297/ -1.297	OL: 1.240/ -1.240	OL: 1.240/ -1.240	OL: 1.242/ -1.242	OL: 1.385	OL: 1.426
	IL: 0.746/ -0.746	IL: 0.000	IL: 0.669/ -0.669	IL: 0.676/ -0.676	IL: 1.098	IL: 1.096
5	SL: 0.198/ -0.198	SL: 1.549/ -1.549	SL: 1.533/ -1.533	SL: 1.528/ -1.528	SL: 1.569/ -1.571	SL: 1.625
	OL: 1.391/ -1.391	OL: 1.367/ -1.367	OL: 1.352/ -1.352	OL: 1.357/ -1.357	OL: 1.445	OL: 1.485
	IL: 0.892/ -0.892	IL: 0.000	IL: 0.838/ -0.838	IL: 0.843/ -0.843	IL: 1.176	IL: 1.175

TABLE V. Magnetic moments of the inequivalent Ni atoms (in μ_B) for *Cmmm*-La₃Ni₂O₇-1313 for the different magnetic states depicted in Fig. 3 as a function of U .

U (eV)	DSA	SL: AFM	SL: AFM	SL: AFM	SL: AFM	SL: FM
		TL: AFM/0/AFM	TL: AFM-C	TL: AFM-G	TL: FM	TL: FM
3	SL: 0.279/ -0.279	SL: 1.399/ -1.399	SL: 1.403/ -1.403	SL: 1.394/ -1.394	SL: 1.443/ -1.443	SL: 1.558
	OL: 1.174/ -1.174	OL: 1.078/ -1.078	OL: 1.075/ -1.075	OL: 1.084/ -1.084	OL: 1.326	OL: 1.362
	IL: 0.523/ -0.523	IL: 0.500/ -0.500	IL: 0.481/ -0.481	IL: 0.463/ -0.463	IL: 0.904	IL: 0.835
4	SL: 0.409/ -0.409	SL: 1.495/ -1.495	SL: 1.481/ -1.481	SL: 1.479/ -1.479	SL: 1.522/ -1.522	SL: 1.609
	OL: 1.297/ -1.297	OL: 1.269/ -1.269	OL: 1.217/ -1.217	OL: 1.222/ -1.222	OL: 1.393	OL: 1.431
	IL: 0.655/ -0.655	IL: 0.009/ -0.009	IL: 0.655/ -0.655	IL: 0.647/ -0.647	IL: 1.077	IL: 1.081
5	SL: 0.495/ -0.495	SL: 1.565/ -1.565	SL: 1.552/ -1.552	SL: 1.554/ -1.554	SL: 1.581/ -1.581	SL: 1.657
	OL: 1.419/ -1.419	OL: 1.378/ -1.378	OL: 1.336/ -1.336	OL: 1.338/ -1.338	OL: 1.455	OL: 1.487
	IL: 0.699/ -0.699	IL: 0.114/ -0.114	IL: 0.810/ -0.810	IL: 0.805/ -0.805	IL: 1.156	IL: 1.152

Appendix D: Further details of the spin-polarized calculations

The magnetic moments obtained for each of the magnetic configurations described in the main text (for $U = 3, 4$ and 5 eV) both for *Cmmm* and *Imma* symmetry are shown in Tables IV and V. The energetics for different magnetic configurations for a *Cmmm* structure (analog to those shown in the main text for *Imma* symmetry) can be seen in Fig. 7. The magnetic ground state in *Cmmm* symmetry is identical (SL: AFM, TL:FM).

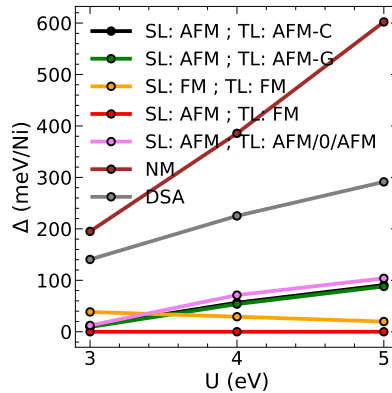


FIG. 7. Energetics of different magnetic configurations depicted in the main text for *Cmmm*-La₃Ni₂O₇-1313 as a function of U .

Appendix E: Unfolded electronic band structure of the magnetic ground state of $\text{La}_3\text{Ni}_2\text{O}_7\text{-1313}$

Fig. 8 shows the unfolded electronic band structure of the magnetic ground state (SL:AFM ; TL:FM) of $\text{La}_3\text{Ni}_2\text{O}_7\text{-1313}$ for the majority spin channel. The bands are obtained by using the KPROJ package [79, 80]. The method implemented in KPROJ uses the projection scheme under which each $|k_i, \epsilon_i\rangle$ eigenvalue from the folded Brillouin zone is projected to the $|K_j, E_j\rangle$ eigenvalue of the primitive Brillouin zone. The method gives the overlap in terms of weights which are plotted in the form of spectral functions. The bands are very similar to those of $\text{La}_4\text{Ni}_3\text{O}_{10}$ [76] apart from the reduced bandwidth due to confinement effects.

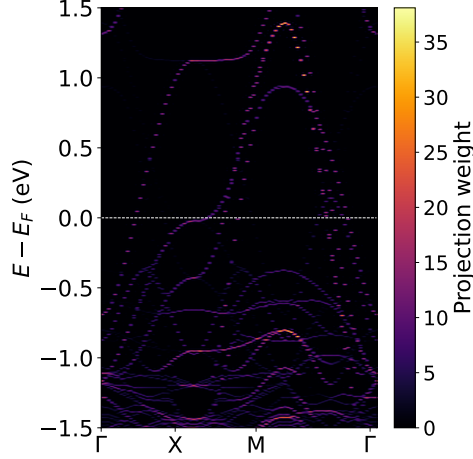


FIG. 8. Unfolded electronic band structure of $\text{La}_3\text{Ni}_2\text{O}_7\text{-1313}$ in the magnetic ground state described in the main text (SL:AFM ; TL:FM).